Title

Local ionic transport enables selective PGM-free bipolar membrane electrode assembly

Journal

Nature Communications, 15(1)

ISSN

2041-1723

Authors

Li, Mengran

Lees, Eric W

Ju, Wen

et al.

Publication Date

2024-09-01

DOI

10.1038/s41467-024-52409-z

nature communications

Article

https://doi.org/10.1038/s41467-024-52409-z

Local ionic transport enables selective PGM-free bipolar membrane electrode assembly

Received: 13 February 2024

Accepted: 5 September 2024

Published online: 19 September 2024

Check for updates

Mengran Li[1,2,10] ✉, Eric W. Lees[3,4,10], Wen Ju[5,6,10], Siddhartha Subramanian[1], Kailun Yang[1], Justin C. Bui[7,8], Hugo-Pieter Iglesias van Montfort[1], Maryam Abdinejad[1,9], Joost Middelkoop[1], Peter Strasser[5], Adam Z. Weber[3], Alexis T. Bell[7,8] & Thomas Burdyny[1] ✉

Bipolar membranes in electrochemical CO_2 conversion cells enable different reaction environments in the CO_2-reduction and O_2-evolution compartments. Under ideal conditions, water-splitting in the bipolar membrane allows for platinum-group-metal-free anode materials and high CO_2 utilizations. In practice, however, even minor unwanted ion crossover limits stability to short time periods. Here we report the vital role of managing ionic species to improve CO_2 conversion efficiency while preventing acidification of the anodic compartment. Through transport modelling, we identify that an anion-exchange ionomer in the catalyst layer improves local bicarbonate availability and increasing the proton transference number in the bipolar membranes increases CO_2 regeneration and limits K^+ concentration in the cathode region. Through experiments, we show that a uniform local distribution of bicarbonate ions increases the accessibility of reverted CO_2 to the catalyst surface, improving Faradaic efficiency and limiting current densities by twofold. Using these insights, we demonstrate a fully platinum-group-metal-free bipolar membrane electrode assembly CO_2 conversion system exhibiting <1% CO_2/cation crossover rates and 80-90% CO_2-to-CO utilization efficiency over 150 h operation at 100 mA cm^{-2} without anolyte replenishment.

Carbon dioxide (CO_2) electrolysis is a promising technology for converting CO_2 electrochemically into valuable products such as carbon monoxide (CO) and hydrocarbons. Despite tremendous advances in achieving industrially applicable rates (up to and over 1 A cm^{-2})[1–5], one of the formidable challenges faced by this technology is fundamentally unstable cell system designs[6–10]. The state-of-the-art membrane electrode assemblies (MEAs) for CO_2 electrochemical reduction are primarily based upon monopolar ion-exchange membranes (IEM), such as cation-[11–13] or anion-exchange[14–16] membranes (CEM or AEM), where the ionic current relies on the transport of either cations or anions. However, monopolar-ion transport causes significant pH deviation from the initial anolyte conditions due to CO_2 acidification and carbon crossover[17–19]. Specifically, under high-rate CO_2 electrolysis, monopolar IEM-based systems result in a substantial loss of feed

[1]Department of Chemical Engineering, Delft University of Technology; 9 van der Maasweg, Delft 2629HZ, the Netherlands. [2]Department of Chemical Engineering, The University of Melbourne, Melbourne, VIC 3010, Australia. [3]Energy Technologies Area, Lawrence Berkeley National Laboratory, Berkeley, CA 94720, USA. [4]Department of Chemical and Biological Engineering, The University of British Columbia, 2360 East Mall, Vancouver, BC V6T 1Z3, Canada. [5]Chemical Engineering Division, Department of Chemistry, Technical University Berlin, Berlin 10623, Germany. [6]Department of Electrochemistry and Catalysis, Leibniz Institute for Catalysis, 18059 Rostock, Germany. [7]Chemical Sciences Division, Lawrence Berkeley National Laboratory, Berkeley, CA 94720, USA. [8]Department of Chemical and Biological Engineering, University of California Berkeley, Berkeley, CA 94720, USA. [9]Department of Chemical Engineering, Massachusetts Institute of Technology, Cambridge, MA 02139, USA. [10]These authors contributed equally: Mengran Li, Eric W. Lees, Wen Ju.
✉e-mail: aaron.li1@unimelb.edu.au; t.e.burdyny@tudelft.nl

CO_2 (e.g., >50% for CO production) due to (bi)carbonate (HCO_3^-/CO_3^{2-}) formation, transport, and eventual regeneration at the opposite electrode[6,17,18,20–22].

The natural tendency for the anodic environment to shift towards neutral pH with monopolar membranes necessitates the use of anode materials based on platinum-group metal (PGM) elements, such as iridium and ruthenium oxides, to maintain efficient and stable kinetics for water oxidation[9]. However, the demand for PGMs needed to scale CO_2 electrolysis up to practical gigawatt levels is prohibitive from both economic and scarcity perspectives unless the PGMs can be limited to <0.1 mg cm^{-2} or > 90% recycled[23]. To allow for the use of a PGM-free anode, one must frequently replenish the alkaline anolyte to resist steady anode acidification[24]. Alkaline electrolytes such as KOH, however, are themselves electrochemically manufactured from KCl via chlor-alkali processes[25], so the required alkaline electrolyte replenishment rate would be equivalent to the CO_2 reduction rates and necessitate substantial electrolyte and water turnover.

Salt precipitation also poses a challenge at the cathode. In AEM-based systems, critical stability issues result from excessive cation crossover and (bi)carbonate salt accumulation, which can precipitate at the gas channels and block CO_2 transport to the active sites[8,10,26–28]. This issue can be relieved to different extents by recently proposed techniques, such as periodic water flushing[14,29], pulsed operation[30], or process optimization (e.g., increased temperature or decreased anolyte concentration)[14,31,32], but these cannot completely mitigate the phenomenon. Use of a CEM and acidic media might resolve the carbonation issue by supplying protons to convert (bi)carbonate back to CO_2[33,34]. However, the proton flux across the CEM may supply excess protons at the cathode that promote the unwanted hydrogen evolution reaction (HER) that outcompetes the desired CO_2 reduction[35,36]. Modulation of the catalyst reaction environment in acidic media may facilitate higher CO_2 selectivity[12], nevertheless, the acidic anolyte conditions will still necessitate iridium-based anodes for water oxidation. Lastly, pure water-fed systems have been demonstrated[2,37]. However, due to the lower electrolyte conductivity, these systems typically show substantially larger cell potentials than those with low concentration electrolytes.

A system configuration based on bipolar membranes (BPM), as depicted in Fig. 1a, provides a promising avenue for maintaining a stable alkaline condition for PGM-free anode and generating a current-dependent proton flux to ameliorate (bi)carbonate formation (Fig. 1b) at the cathode[38–43]. The BPM comprises a cation-exchange layer (CEL) and an anion-exchange layer (AEL), with their interface (bipolar junction) dissociating water into H^+ and OH^- (Fig. 1c) when operated in reverse bias[44]. As a result, the BPM can supply current-dependent fluxes of protons to the cathode and OH^- to the anode, thus inherently maintaining a stable pH difference at both cathode and anode during electrolysis while limiting ion crossover. BPM-based systems, if operated well, can sustain high anodic alkalinity to allow the use of PGM-free anode (e.g., nickel-based anode[45]) and utilize protons to revert (bi)carbonate to CO_2, thus preventing salt precipitation (Fig. 1b) and increasing CO_2 utilization.

At present, however, it remains challenging to achieve an efficient and stable PGM-free BPMEA cell, which requires well-controlled local ionic transport and chemical reactions. Importantly, CO_2 crossover through the membrane should be eliminated to avoid anolyte pH

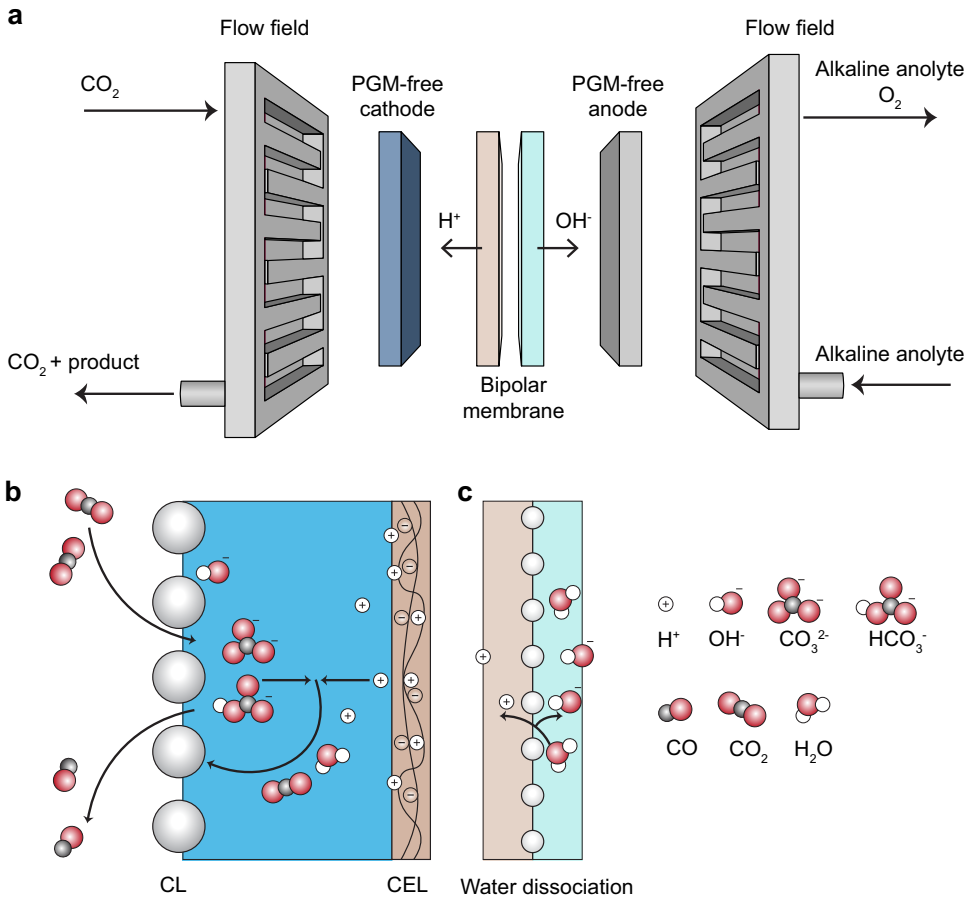

Fig. 1 | Illustration of an ideal BPM-based membrane electrode assembly for CO_2-to-CO electrolysis. a A schematic illustration of an ideal BPMEA cell configuration. **b** Elucidation of the use of the reverted CO_2 from (bi)carbonate acidification for CO_2 reduction at the interface between the cathode and cation-exchange layer (CEL). **c** Water dissociation at the interface between CEL and anion-exchange layer (AEL).

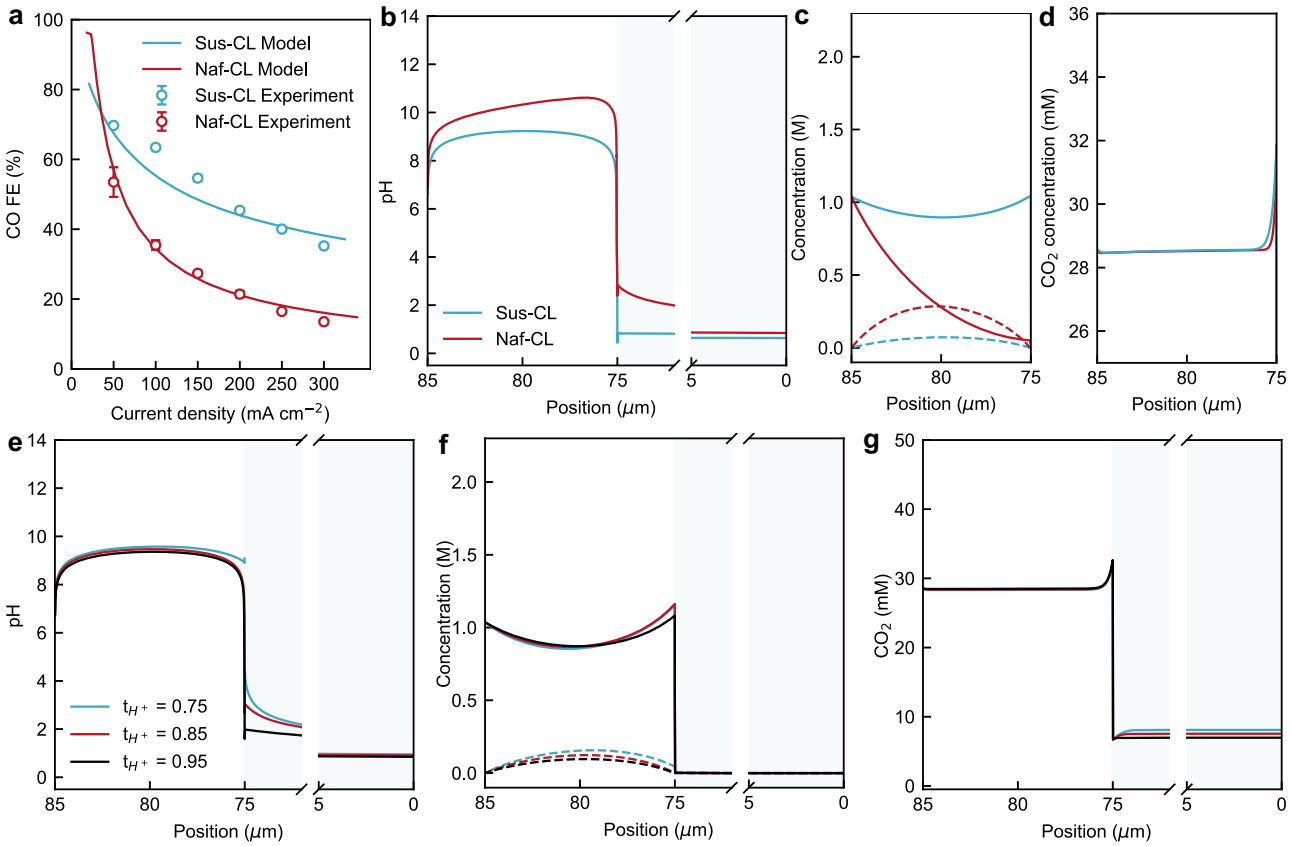

Fig. 2 | 1D continuum modelling results of the BPMEA. a Modelled and experimental Faradaic efficiencies of CO for catalyst layer (CL) incorporated with Sustainion (Sus-CL) or Nafion (Naf-CL) as a function of current densities. Comparison of **b** pH, **c** (bi)carbonate concentrations, and **d** CO_2 local concentration across CLs at 100 mA cm^{-2}. Profiles of **e** pH, **f** (bi)carbonate ions, and **g** CO_2 local concentration across CEL and Sus-CL as a function of proton transference numbers. The bipolar junction is located at x = 0 μm, and the CEL|CL is located at x = 75 μm. The concentration profiles of the CEL for **c** and **d** are presented in Supplementary Fig. S2, and not shown here for clarity.

neutralization and allow the use of a PGM-free anode, such as nickel. Meanwhile, alkali cation crossover should be controlled within a range sufficient for the activation of CO_2 reduction, but limited enough to prevent excessive salt precipitation at the cathode[40].

Poor management of the local ionic transport and reactions within the catalyst layer usually entails undesired HER and thus low selectivity for CO_2 reduction at the cathode due to the high availability of protons close to the catalyst that appear to be more easily reduced[40,46]. Product selectivity can be improved by either introducing a stagnant catholyte layer at the cathode/CEL interface[38,41] or applying an acid-tolerant and selective catalyst[39,42]. The abundant cations in the catholyte layer can activate CO_2 reduction but may cause salt precipitation[41]. Recent reports[39,42] have also shown that acid-tolerant catalysts, such as molecular or metal-nitrogen-carbon catalysts, are more selective than silver catalysts for CO_2 reduction due to their weak binding with protons[47–49] but remain far inferior to monopolar IEM-based systems.

This work reported here uses a combined theoretical and experimental approach to understand the scientific challenges central to BPMEA systems and presently impede their prospects. The results unveil that the ion transference number of the membrane and local ion transport within the catalyst layers serve a pivotal role in eliminating counterion crossover and maximising accessibility of the catalyst surface to the reverted CO_2. The insights provided by our work can guide the rational design of BPM-based electrochemical systems.

Results

To understand the local ion transport in a BPMEA, a 1D isothermal continuum model was developed based on previous work by Weng et al.[50] and Lees et al.[51]. The model domain includes an ionomer-impregnated porous cathode catalyst layer (CL) and CEL of the BPM. The catalyst layer consists of nickel-nitrogen-carbon catalyst (NiNC-IMI) mixed with either cation- (Nafion, a sulfonated fluoropolymer[52]) or anion-exchange ionomer (Sustainion, an imidazolium functionalized styrene polymer[31]). The model was fit to the experimental CO Faradaic efficiency data collected from NiNC-IMI catalyst layers with Sustainion ionomers by adjusting the electrochemical parameters such as the transfer coefficients and exchange current densities for CO_2 reduction and the competitive HER (see Fig. 2a). To validate the model, the same kinetic parameters were then used to predict the CO Faradaic efficiency data collected with the Nafion ionomer. Details of the models (e.g., equations, boundary conditions, and parameters) are described in the Supplementary Information.

Since previous work has shown the role of anolyte ion concentration and crossover on cathodic performance and stability in a BPMEA CO_2 electrolyzer[40], we used the model to more deeply investigate two strategies to control the ionic transport within the cathode. Specifically, (i) the use of ionomer in the CL for selective ionic transport and (ii) promoting an increased proton transference number in the CEL. Including ionomer in the catalyst layer is a common and effective approach to modulate local ionic transport. Further, maintaining a high proton flux from the CEL to the cathode is also a prerequisite for a stable and efficient BPMEA system. Near-unity water dissociation efficiencies are desired as they limit ionic interactions between the anode and cathode environments that can impact anolyte pH and salt precipitation at the cathode. Therefore, these two strategies are perceived as practical approaches to

managing local ion transport and thus reaction microenvironment in the electrolysis cell.

We first examined the role of ionomer choice for the CL in determining local ionic concentrations in the catalyst layer. As presented in Fig. 2b, c, incorporating anion-selective Sustainion ionomer in the CLs (Sus-CLs) leads to a counterintuitively lower pH and CO_3^{2-} concentration than the Nafion ionomer in the CL (Naf-CLs). Notably, the Sus-CLs case provided a substantially higher (7 folds) HCO_3^- concentration near the CEL|CL interface, and over the entire catalyst layer an average HCO_3^- concentration that is more than twice that of the Naf-CLs case. This discernible divergence is a result of the different fixed charges of the two ionomers. Anion exchange ionomers promote the transport of generated (bi)carbonates from the cathode towards the BPM, while the Nafion rejects this transport and promotes an increased (bi)carbonate concentration near the generation point. The positive fixed charge of the Sus-CLs then provides ample HCO_3^- available for acidification and CO_2 regeneration near the CEL|CL interface.

In addition to the anion transport, it is important to assess the cation transport (H^+ and K^+). As further suggested from the calculated K^+ profiles shown in Supplementary Fig. S3a, the positively charged quaternary ammonium groups in the ionomer at least partially exclude K^+ transport from CEL to CL in the Sus-CLs and thus likely contribute to the observed reduced pH in the CLs by lowering the required amount of OH^- ions needed to balance the positive charge. By contrast, the concentration profiles predicted for Naf-CL indicate a more uneven ionic distribution as compared to Sus-CL. The negatively charged sulfonic groups in Nafion lead to an excessive amount of K^+ in the Naf-CL (see Supplementary Fig. S3a), which then fosters a high content of OH^- (or high pH shown in Fig. 2b) and CO_3^{2-} to maintain charge neutrality.

Overall, both ionomer cases show the ability for CO_2 that is converted to (bi)carbonates to be regenerated into CO_2 by the proton flux from the CEL of the BPM. Interestingly, the concentration of HCO_3^- at Naf-CL shown in Fig. 2c decreases from around 1.0 M at CL|GDL interface down to 0.047 M at the CEL|CL interface. Such a steep decrease in HCO_3^- concentration is a result of increased local pH inside Naf-CL. Due to the high local pH inside Naf-CL (Fig. 2b), however, the regenerated CO_2 tends to diminish and convert back into CO_3^{2-} within the Naf-CL (Fig. 2c). As such, the uneven ionic distribution in Naf-CL might not be ideal for an efficient electrochemical conversion of CO_2 because it could cause a low utilisation efficiency of the reverted CO_2 for electrochemical conversion. Similarly, the local CO_2 concentration near the Sus-CL|CEL interface is slightly higher than Naf-CL|CEL interface (Fig. 2d) due to a higher concentration of HCO_3^- which promotes CO_2 regeneration. However, the CO_2 concentration throughout the bulk of the CL is similar for the Sus-CL and Naf-CL because of the constant excess CO_2 supply provided at the CL|GDL interface.

Next, we use the Sus-CL model to investigate the impact of H^+ transference number on the local ionic transport across the CLs. The ionic conduction across the CEL|CL interface relies on the transport of H^+, K^+, and (bi)carbonate ions, with H^+ being the primary charge carrier. The H^+ transference number quantifies the fraction of current associated with H^+ transport across the CEL. The total ionic current is the sum of the H^+ transport, K^+ crossover from the anode, and anion crossover from the cathode. By sweeping the H^+ transference number from 0.75 to 0.95, as presented in Fig. 2e–g and Supplementary Fig. S3b, we observed a decrease in pH, K^+ and CO_3^{2-} concentrations but an increase in HCO_3^- concentrations in the CLs. This trend is as expected because an increase in H^+ transference number indicates a suppressed current associated with K^+ cations and promotes carbonate acidification within the CLs. Additionally, as shown in Fig. 2g, increasing the H^+ transference number does not notably increase the local CO_2 concentration but reduces the CO_2 concentration within the CEL due to the minimised (bi)carbonate crossover from CL to CEL. The downside of an increased H^+ flux across CEL|CL interface could be HER out competing CO_2 reduction through direct H^+ reduction and limited cations available to activate CO_2 electrochemical reduction.

The role of ionomer in CL on BPMEA performance

To validate the predictions of the model, we compared experimentally NiNC-IMI CLs prepared with Sustainion and Nafion ionomers. A comprehensive study of the NiNC-IMI catalyst has been published elsewhere[53,54], so this study will focus on the role of the ionic transport in the CLs on the BPMEA performance by using the NiNC-IMI as a model CL. The products from the BPMEA cells are primarily CO and H_2 with minor formate or formic acid (see nuclear magnetic resonance results in Supplementary Fig. S4a). Because the BPM is effective in minimizing formate crossover to the anolyte[55], it is challenging to calculate the formate FEs accurately by analysing anolyte compositions. Hence, this work focuses mainly on the CO and H_2 products from the electrolysis.

Figure 3b–d shows that the ionomer in the CL defines cathode activity and selectivity in the BPMEA configuration. 15 wt% Sustainion ionomer in the CL can profoundly improve the catalyst CO FE and partial current densities compared to the 15 wt% Nafion. Due to the different equivalent weight of the ionomers (1100 g/mol for Nafion; ~225 g/mol for Sustainion[31]), 15 wt% Sustainion contains approximately five times the concentration of ionic groups as compared to the 15 wt% Nafion. Considering the reported minor effects of ion-exchange capacities on selectivity and stability of NiNC CLs[53], this study chose the CLs with these ionomer loadings are used as model electrodes. As shown in Fig. 3b, the CO FE is 69.7 ± 0.5% at 50 mA cm^{-2} and 45.4 ± 0.5% at 200 mA cm^{-2} for CLs with 15% Sustainion ionomer, much higher than the CLs based with Nafion (53.5 ± 4.2% at 50 mA cm^{-2} and 21.4 ± 1.0% at 200 mA cm^{-2}). The Naf-CLs reach a CO limiting current density of ~ 41 mA cm^{-2}, more than two-fold lower than the Sus-CLs (>105 mA cm^{-2}).

When compared with those reported in the literature, as shown in Supplementary Fig. S5 and Supplementary Table S1, the BPMEA cells using CLs with 15% Sustainion ionomer, as studied in this work, show the lowest cell voltages and are among the best reported CO partial current densities at cell voltages below 4 V. It is interesting to note that, regardless of the catalyst and polymer materials used in the CLs, the NiNC-IMI CLs with 15% Sustainion ionomer show the same CO partial current densities - cell voltage relations to the CLs based on cobalt tetraaminophthalocyanine catalysts grafted on the positively charged polymer, as very recently reported by Li et al.[56]. Both cases are superior in CO partial current densities to most of the reported CLs based with Nafion[41,42,46,57,58] or no ionomers[40] for BPMEAs at below 4 V cell voltages. Such similarity in these two positively charged CLs indicate that, the CO production rate at relatively low cell voltages should be strongly correlated with the presence of positively charged polymer (i.e., Sustainion ionomer or other positively charged polymer) in the CLs, which exerts a profound impact on the ionic transport.

Therefore, the notable enhancement in CO_2-to-CO upon FEs and partial current densities is related to the local mass transport within the CLs that either improves the local concentration of CO_2 or limits the local concentration of protons. Supplementary Fig. S6 demonstrates no significant suppression of HER by the Sustainion ionomer, implying a similar local proton availability and/or catalytic HER activity in both cases. Hence, we postulate that the observed improvement likely originates from the enhanced bicarbonate local transport within Sustainion-based CLs, as predicted from our model in Fig. 2c. The increase in local bicarbonate concentration in the CL provides an even CO_2 distribution in the CL and thus promote CO_2 electroreduction.

In the BPMEA reported here, there are two sources of CO_2: CO_2 that dissolves from the gas feed and CO_2 that is regenerated from bicarbonate via acid-base chemistry. The modelled CO_2 concentration profiles (Fig. 2c, f) show that the potent proton flux from the CEL yields a peak in CO_2 concentration at the CEL|CL interface. The increased CO_2

https://doi.org/10.1038/s41467-024-52409-z

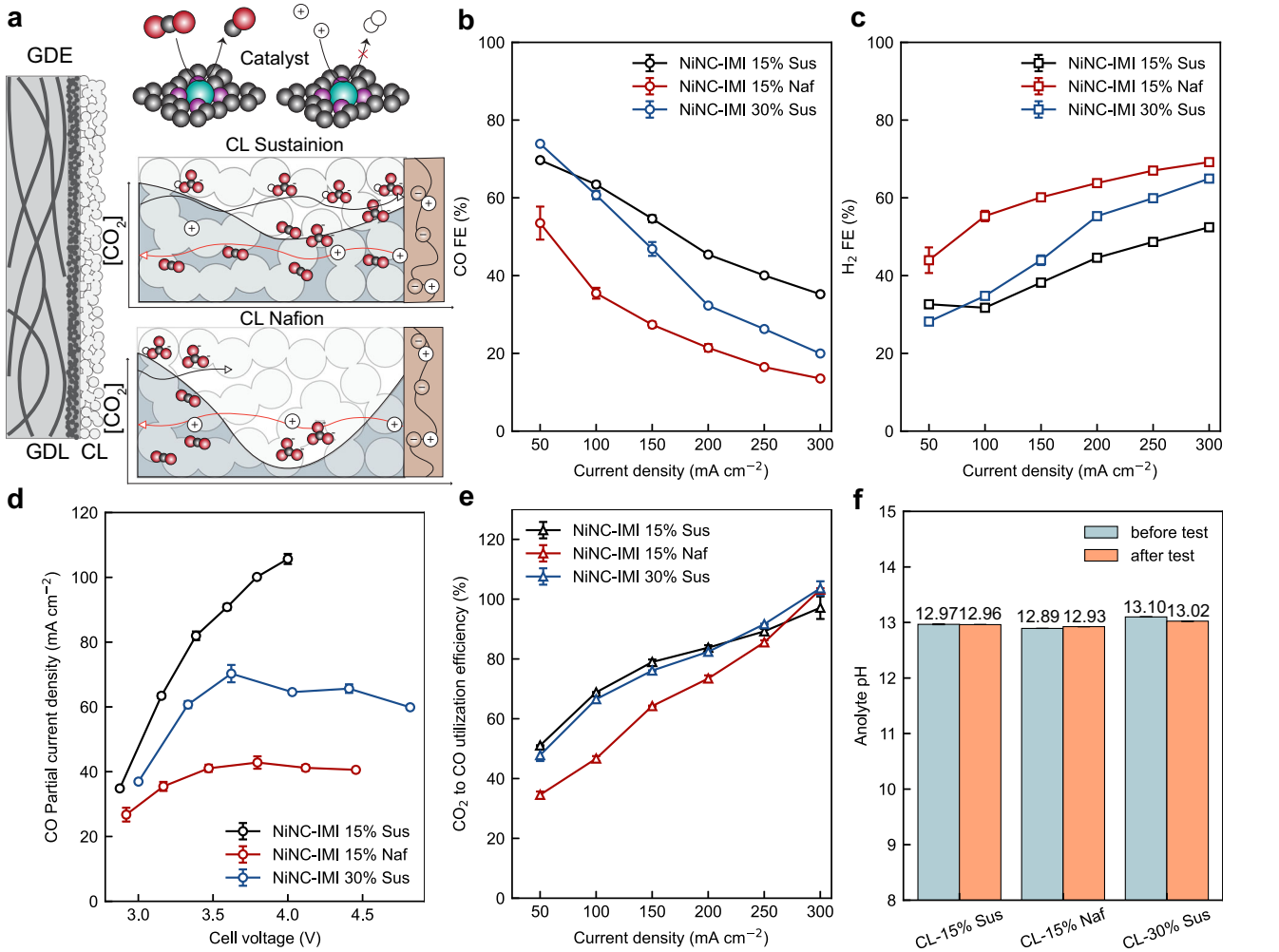

Fig. 3 | Comparison of catalyst layers for CO_2 reduction to CO in BPMEA cells. **a** Schematic illustration of the CL on a gas-diffusion layer (GDL), the catalyst materials, and the importance of the migration of (bi)carbonate across the Sustainion-based CL for CO_2 local regeneration. Faradaic efficiency of **b** CO and **c** hydrogen of the CLs versus total current densities. **d** CO partial current density and **e** CO_2-to-CO utilization efficiency over CLs. **f** pH changes of 100 mL 0.1 M KOH aqueous anolyte as a function of CLs before and after cell tests (6300C total charge) under 50–300 mA cm^{-2}. The error bar represents standard deviations over at least three tests.

concentration results in an increase in the predicted CO_2 flux and CO partial current density near the CEL|CL interface as shown in Supplementary Fig. S7. This result is consistent with our previous bicarbonate electrolyser model that shows high CO formation rates at the CEL|CL interface[51]. In this BPMEA model, a high rate of CO formation is also observed at the CL|GDL interface. This difference is attributed to the additional CO_2 source from the gas phase, which is absent in the bicarbonate electrolyser. These modelling results confirm that both regenerated and dissolved CO_2 contribute to CO production in a BPMEA.

Since bicarbonate anions exhibit more facile transport in the anion-exchange Sustainion ionomer than the cation-exchange Nafion ionomer[18] (see Fig. 2b), we predict that the Sustainion ionomer should allow a facile transport of bicarbonate anions for CO_2 regeneration, providing ample local CO_2 for electrochemical conversion across the CL structure (see Fig. 3a). By contrast, in the Naf-CL, the regenerated CO_2 tends to be spatially localized, causing a limited proportion of catalyst surface in the CLs to be accessible by the regenerated CO_2. Therefore, the even distribution of bicarbonate enables the Sustainion-based CL with a larger catalyst surface area accessible by the regenerated CO_2 than a Nafion-based CL[59]. Thus, while both systems enable reasonable CO_2 utilization efficiencies, Sus-CL case exhibits both higher CO_2 utilization efficiencies, CO FE, and partial current densities at comparable cell voltages (Fig. 3d).

Figure 3e shows that the CO_2-to-CO utilisation efficiency increases with current density. Here, the CO_2-to-CO utilisation efficiency is defined as the ratio of the CO_2 reduced to CO versus the total CO_2 consumed in the cell (i.e., due to crossover and reaction). The observed CO_2-to-CO utilisation trend as a function of current density could result from an increase in the H^+ transference number across the CEL of the BPM, because water dissociation dictates the overall ionic current while the co- and counter-ion crossover is mass-transport limited at increased current densities[60]. When one mole of CO is produced, for example, there will be two moles of electrons consumed, two moles of H^+/K^+ transported from the CEL, and two moles of OH^- co-produced. The OH^- can then be converted into one-mole carbonate or two moles of bicarbonate, which require two moles of protons to remove the (bi)carbonate species. Therefore, the H^+ transference number determines the availability of the H^+ to revert the generated (bi)carbonate species back to CO_2. As the H^+ transference number is always below 1, it means that some CO_2 converted to (bi)carbonates are never recovered and will either precipitate at cathode or crossover to the anode at periodic intervals. Consequently, a high H^+ transference number across the BPM is beneficial to lowering the local pH and

https://doi.org/10.1038/s41467-024-52409-z

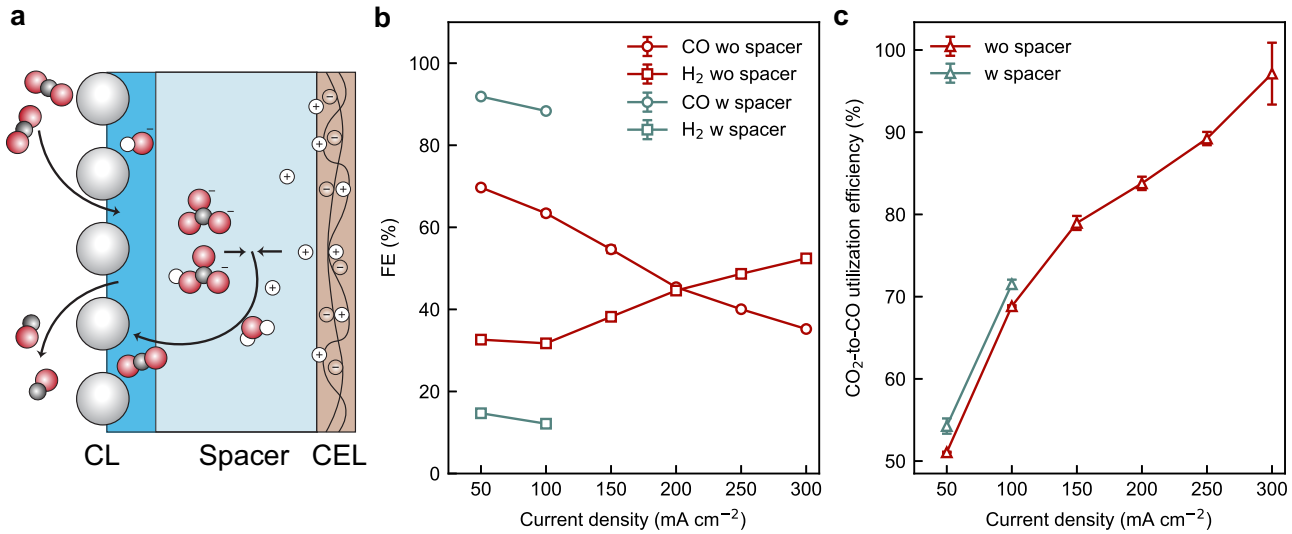

Fig. 4 | The effects of the cathode/CEL spacer on the performance of the BPMEA cell. a A schematic of the spacer at the cathode/CEL interface. Comparison of the **b** CO Faradaic efficiency and **c** CO_2-to-CO utilisation efficiency versus total current densities of the BPMEA with and without the spacer. The BPMEA cell used cathodes with NiNC-IMI catalyst with 15% Sustainion ionomer as the catalyst layer. The error bar represents standard deviations over at least three tests.

regenerating CO_2 from (bi)carbonate, hence, maximizing CO_2-to-CO utilisation efficiency.

Therefore, the CO_2-to-CO utilisation efficiency could serve as an indicator for the availability of reverted CO_2 for electrochemical conversion in the CLs. As shown in Fig. 3e, both CLs based with 15 wt% and 30 wt% Sustainion ionomer exhibit higher CO_2-to-CO utilisation efficiency than the ones with Nafion ionomer at current densities below 250 mA cm^{-2}. This experimental observation further confirms the beneficial effect of Sustainion ionomer in improving local availability of the reverted CO_2 accessible by the catalysts for electrochemical conversion.

A further increase of Sustainion ionomer loading to 30 wt% in the CL lowered the FEs and limiting current density for CO production. (Fig. 3b–d) Such decline in performance is likely attributable to the blockage of the CL pores and reactive sites by the ionomer itself, resulting in an increased diffusion length for CO_2 gas from gas channels to the catalyst surface or loss of active surface in the CLs, respectively. However, the CO_2-to-CO utilisation efficiency is not significantly impacted by the increment of the ionomer loading, implying that in-situ formed (bi)carbonate ions can be reverted to CO_2 easily within the CL matrix.

More importantly, as shown in Fig. 3f, the anolyte shows only a slight decrease in pH after the cell testing, with a total charge of 6300 C passed through the cell during the test. The pH of the anolyte could have been decreased because of both carbon crossover from the cathode to the anode and cation crossover from the anode to the cathode. The minimal change in the anolyte pH is due to the unique BPM function, which supplies protons at the cathode to convert (bi) carbonate anions to CO_2 for CO production and minimises ion crossover rates across the cell. This feature allows BPMEA cells to be operated stably using a PGM-free anode based on nickel and with a high CO_2-to-product utilisation efficiency, which could not be easily done using monopolar membrane-based electrolysis cells.

The role of the H^+ transference number on BPMEA performance

The role of proton transference number is investigated experimentally by examining the effect of K^+ cation crossover on CO_2 reduction using 0.1 M and 1 M KOH as the anolyte. A concentrated KOH is expected to accelerate the crossover rate of K^+ due to the large concentration gradient across the membrane (see Supplementary Fig. S8a). Because cations are essential in activating CO_2 reduction, the results in Supplementary Fig. S8b show that 1 M KOH anolyte can slightly improve CO FE at current densities >150 mA cm^{-2}. This finding is consistent with our previous report highlighting the cations' vital role in enhancing CO FEs over silver electrodes[40]. Supplementary Fig. S8c suggests that the BPMEA cell with a dilute anolyte shows a higher CO_2-to-CO utilisation efficiency than the concentrated anolyte. This trend matches our model predictions of the proton transference number in Fig. 2d–f, because a reduced K^+ crossover rate achieved by using a dilute anolyte leads to an increase in proton transference number and acidification of (bi)carbonate within the CL. Therefore, a trade-off exists between product selectivity and CO_2 utilisation efficiency when choosing the anolyte for the BPMEA cell.

Local H^+ enrichment at CEL/CL interface

In addition to the distribution of (bi)carbonate ions within the CL, we studied the local reaction environment at the CEL|CL interface by introducing a hydrophilic porous spacer (65 um thick) between the CL and CEL. (Fig. 4a) This configuration is fundamentally different from the previously reported method[41] by Xie et al. that includes concentrated salts within the spacer. In this study, we applied the spacer pre-soaked with ultrapure water before the cell assembly. The ion conduction within the spacer solely depends on the ionic fluxes of protons, (bi)carbonate anions, and K^+ cations that come from the CEL and anolyte.

As shown in Fig. 4b, the spacer significantly suppresses the HER down to below 15% and boosts the CO FEs up to 91% at 50 mA cm^{-2} and 88% at 100 mA cm^{-2}, which is almost comparable to MEA cells based on monopolar membranes. The comparison of the CO partial current densities vs. cell potentials, as shown in Supplementary Fig. S9, suggests cells with and without spacer achieve similar CO partial current densities under similar cell voltages. Therefore, the observed CO FE enhancement is mainly attributable to the suppression of HER at CL|CEL interfaces. This finding also indicates that the majority of HER in the absence of spacer occurs at the CL|CEL interfaces due to the direct contact of the CL with excess protons; the spacer increases the retention time for protons to reach the catalyst surface, thereby enabling more CO_2 regeneration from (bi)carbonates.

The drawback to including the spacer in the BPMEA cell is the large ohmic loss due to the slow ionic conduction across the spacer, as verified by the electrochemical impedance spectroscopic analyses in Supplementary Fig. S10. The absence of abundant water at the cathode

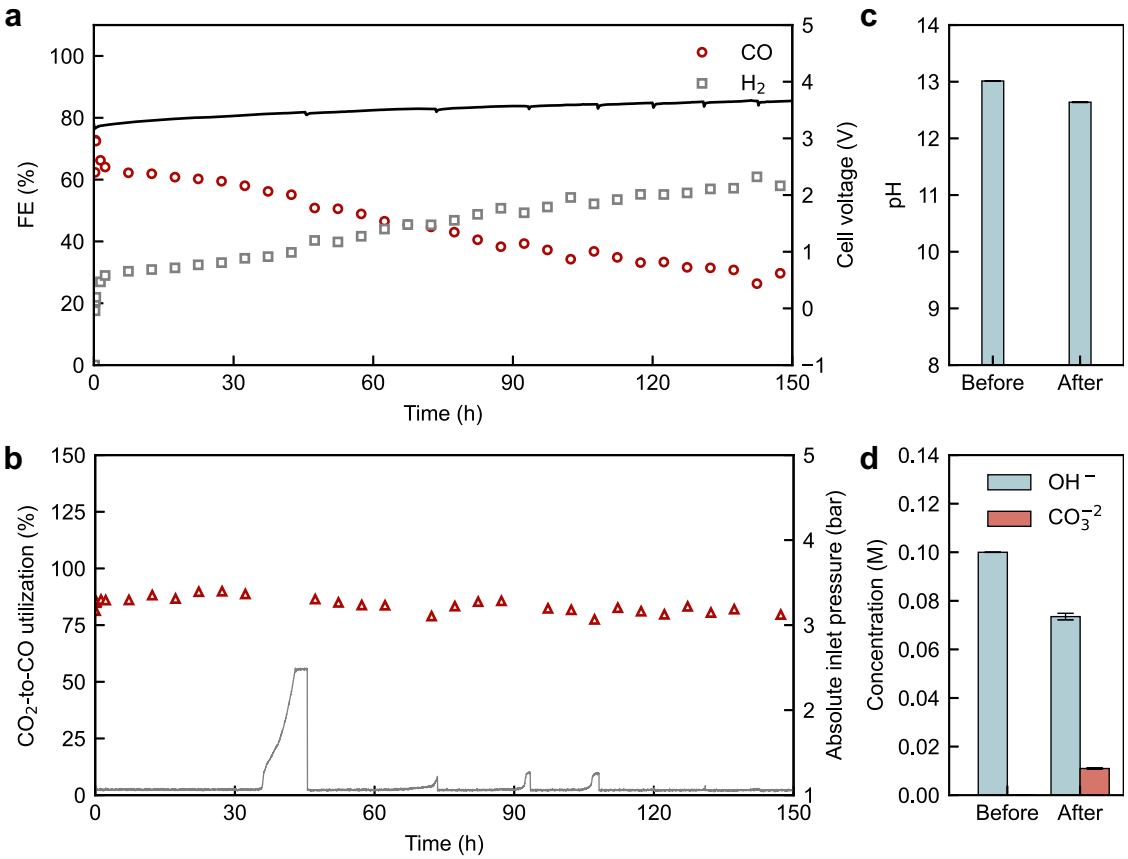

Fig. 5 | Short-term stability of the PGM-free BPMEA cell. a Faradaic efficiency (FE) of gas products and cell potential and **b** CO_2-to-CO utilisation efficiency and inlet pressure of the BPMEA cell as a function of time for the BPMEA cell. Comparison of the **c** pH and **d** anion concentration of the anolyte before and after the stability test. The BPMEA cell was operated at a constant current density of 100 mA cm^{-2}, using 1 L 0.1 M KOH as the anolyte, Ni foam as the anode and NiNC-IMI catalyst with 15% Sustainion ionomer as the cathode CL. The flow rate was 20 sccm for the CO_2 gas inlet and 30 mL min^{-1} for the anolyte. The error bar in **d** represents the stand deviation across more than three tests.

side of the BPMEA accelerates the dehydration of the spacer, which causes further reduction of the ionic conductivity of the spacer and eventually rapid cell voltage overshoot (See Supplementary Fig. S11). Nonetheless, the results highlight the importance of the cell configuration in determining the CO_2-to-CO selectivity of the BPMEA cells.

Effect of ion transport on BPMEA cell voltages

The local ionic transport has an impact on the BPMEA cell voltage. Most of the current BPMEAs require higher cell voltages than monopolar MEAs to drive the same current densities due to the high overpotential for water disassociation (WD) at the bipolar junction. Recent reports have indicated that WD kinetics can be effectively improved by using proper catalysts at the bipolar junction[61] and optimising the operating conditions (e.g., increasing temperature)[62], which has been widely discussed in the literature and is beyond the scope of this study. Instead, this study investigates how the local ionic transport across the CLs influences the overall cell voltages.

The electrochemical impedance data (see Supplementary Figs. S12 and S13) shows that the choice of the ionomer in the CL has a significant impact on the ohmic loss of the BPMEA. This result is not surprising because the ohmic resistance is dominated by the ionic transport. As shown in Supplementary Fig. S14a, the CLs with Sustainion consistently show 1–1.34 Ω cm^2 lower ohmic resistance than the CLs with Nafion across the tested current densities. This difference becomes more discernible at high current densities and can be translated into a significant ohmic overpotential of ~0.4 V at 300 mA cm^{-2} (Supplementary Fig. S14b). This improvement can be a result of the much lower ionic conductivity of the Nafion (~30 mS cm^{-1} in KOH at 25 °C)[63] than the Sustainion polymer (~60 mS cm^{-1} under similar conditions)[31].

Additionally, the Nernstian shift, arising from the pH gradient between the cathode and anode, should also serve a role in influencing the observed cell voltages. As it is challenging to determine the pH accurately at the BPMEA cathodes due to the experimental limitations and pH variations across the CL structures, we estimated the impact of the local ionic transport on the Nernstian shift using our models and compared the results in Supplementary Fig. S15. Due to the higher estimated pH over the Naf-CLs (see Fig. 2b as an example), the Nernstian shifts for the Naf-CL case then exerts slightly more negative impact (<0.1 V *c.f.* ~0.4 V difference for ohmic loss) on the overall cell voltages across the tested current densities than Sus-CL cases. This modelling result, together with the impedance analyses discussed above, indicate that the impact of the ionic transport on cell voltages is more closely related to the ionic conductivity of the CLs than the Nernstian shift.

Long-term stability and ion crossover

Finally, we evaluated the long-term stability of the PGM-free BPMEA cell, particularly as it relates to the anolyte pH and the stable use of nickel anodes. Figure 5a indicates that the CO Faradaic efficiency rapidly dropped from 73% to 64% within the first 1.5 h, then decreased linearly to 30% after 150 h at a degradation rate of 0.36% per hour. Meanwhile, the HER increased along with the loss in CO FE. Such discernible selectivity loss likely originates from an increase in the contact area between the catalyst and H^+ and possible deactivation of the catalyst layer in the acidic environment due to the lack of sufficient K^+

in the CLs. Both could contribute to the rise in the rate of HER and suppression of the rate of CO_2 reduction. As long-term stability over 1000 h has been demonstrated very recently in pure water-fed CO_2 electrolysis in MEA, where concentrations of alkali cations are also limited, the stability of the CO_2 reduction over BPMEA should be further improved by implementing the advances in designing alkali-cation-lean CLs, such as the use of novel catalyst layers[37] and charged polymers[2].

The cell voltage also increased at a degradation rate of 0.086% per hour. By comparing the ohmic resistances obtained from electrochemical impedance (Supplementary Fig. S16), we found that the degradation of the cell potential should be related to the increase of the polarization resistance over either the cathode or anode rather than the deterioration of the BPM. On the other hand, as shown in Fig. 5b, the CO_2-to-CO utilisation efficiency increased rapidly in the first 1.5 h and was subsequently sustained at above 80-90% across the measurement. The rapid rise in CO_2 utilisation within the first 1.5 h implies that the rapid drop in CO FE is mainly a result of an increase of proton local availability for HER in the CL.

Without replenishing the anolyte across the entire test, we observed no significant change in the pH value of the anolyte after the test, as shown in Fig. 5c. The titration results shown in Fig. 5d and Supplementary Fig. S17 revealed that about 0.006 mol K^+ cations have migrated to the cathode side, which is equivalent to 0.21 % of the ionic current during the conditioning. Due to the anolyte's high alkalinity, most of the CO_2 crossover is converted to carbonate ions in the anolyte. Figure 5d shows that the anolyte after the test is composed of 0.0735 M OH^- and 0.011 M CO_3^{2-}, implying that the (bi)carbonate crossover contributed to <0.774% of the ionic current. The extremely low K^+ and CO_2 crossover rates were essential in sustaining the Ni-based anode stability without replenishing the anolyte during the 150-h test. We posit that a proton transference number of ~99% was maintained over the course of the experiment. While the 0.21% K^+ crossover is likely needed to maintain CO_2 reduction at the cathode, the 0.774% carbonate crossover is all that needs to be avoided to maintain anolyte pH indefinitely.

After 150 h conditioning within the BPMEA cell, as revealed by the XRD results in Supplementary Fig. S18, the Ni anode remained as metallic Ni, while additional minor phases related to potassium nickelates[64] formed due to the long-term oxidising treatment. Importantly, no nickel carbonate phase was detected in the conditioned anode, implying that the BPMEA configuration stabilised the Ni-based anode. Ex-situ surface analyses further confirm that both fresh and conditioned anodes are predominantly covered with $Ni(OH)_2$ species at the surfaces (Supplementary Fig. S19), and that their structures shown in Supplementary Figs. S20 and S21 remain intact after 150 h conditioning. The retained structural and chemical stability of the Ni anode is a main result of the alkaline local environment achieved by the BPM, which supplies hydroxide ions and suppresses K^+ and CO_2 crossover.

We also noticed that the inlet pressure of the cell rose after an interval of 12-30 h. The rise of the inlet pressure is mainly a result of the build-up of precipitated (bi)carbonate salts at the entrance of the gas channel in the cell, though there was no discernible salt precipitation elsewhere in the gas channels or the back of the cathode (see Supplementary Fig. S22). The salt precipitation occurs typically when the concentration of the local (bi)carbonate exceeds the solubility (e.g., 8.03 M for K_2CO_3 and 3.62 M for $KHCO_3$)[26,28] at the cathode structure and the crystal can grow continuously to reach the gas channels, similar to efflorescence process, due to its hygroscopic and porous nature. The inlet pressure rise (due to the salt precipitation) elucidates that there is a continuous supply of K^+ from the cation crossover of about 0.21% to the cathode for the salt precipitation, which cannot be easily mitigated, especially at a high current density.

To circumvent this issue, we applied ~1 mL pure water pulse to wash off the precipitated salt from the gas channel during operation when an increase in inlet pressure was observed. Unlike the reported hourly water flush to remove the salts at the cathode for the anion-exchange membrane electrode assembly cell[14,29], the BPMEA cell requires a much less frequent water pulse, thanks to its high CO_2 utilisation and controlled K^+ concentrations at the cathode. The water pulse operation also showed negligible impact on the cell potential and CO Faradaic efficiency, as shown in Fig. 5a.

In summary, this combined modelling and experimental work highlights and elucidates the critical role of the local ionic transport and reaction environment in determining the CO_2-to-CO activity, selectivity, and utilisation efficiency in BPM electrode assemblies constructed without platinum group metals. The combined theoretical and experimental results reveal that an even distribution of bicarbonate across cathode catalyst layers enhances the accessibility of the reverted CO_2 to the catalyst layer and thus boosts CO Faradaic efficiency and limiting current densities more than two-fold. We also found that the proton transference number determines the CO_2 utilisation efficiency: a high proton transference number generally achieves a high CO_2-to-CO efficiency but may not necessarily lead to a high CO_2 reduction selectivity. Although hydrogen evolution still outcompetes CO_2 reduction at >150 mA cm^{-2}, our results suggest that hydrogen evolution occurs primarily at the membrane/catalyst interfaces and can be suppressed effectively by the inclusion of a spacer at the interface. Lastly, we demonstrate notably low crossover rates for CO_2 and K^+ (<1% of total charge) over a PGM-free BPMEA cell operating at 100 mA cm^{-2} for 150 h. This cell achieves a 80–90% CO_2-to-CO utilisation efficiency and stable alkalinity in the anolyte. The findings of this work provide new insights into advancing and assessing BPM electrochemical systems via catalyst material design and modulation of local transport and reaction microenvironment.

Methods

One-dimensional modelling

A 1D isothermal continuum model was developed for the cation exchange layer (CEL) and catalyst layer (CL) of the BPM-based CO_2 electrolyser MEA based on previous porous electrode models by Weng et al.[65] and Lees et al.[51] (Supplementary Fig. S1). The CL domain of the model was assumed to be composed of gas, Sustainion or Nafion ionomer, and solid NiNC-IMI catalyst phases with constant volume fractions of 0.37, 0.43, and 0.2, respectively. These values correspond to the volume fractions of the ionomer and catalyst in the ink precursor. The CEL domain was assumed to be impermeable to gas transport and composed entirely of Sustainion ionomer. Supplementary information provides a detailed description of the governing equations, effective diffusion coefficients, boundary conditions, and Donnan equilibriums for the models.

Imidazolate-derived Ni-N-C catalyst synthesis

The imidazolate-derived Ni-N-C (NiNC-IMI) catalyst for the cathode was synthesized following the reported approach[54]. Briefly, we first mixed 0.03 mol $Ni(NO_3)_2.6H_2O$ (equivalent to 8.724 g) with 24 g imidazole compound in 600 mL deionized water, and then added 1200 mL 0.3 M NaOH solution into the mixture with a dosing rate of 60 mL min^{-1}. After stirring the solution for 6 h, we collected the solids via vacuum filtration, washed till the filtrate reached pH neutral, and finally freeze-dried. We annealed the dried sample under flowing nitrogen (~ 80 mL min^{-1}) at 800 °C for 3 h at a ramping rate of 5 °C min^{-1}, soaked the annealed sample in 200 mL ~1 M H_2SO_4 stirred for 10 h, washed the acid-treated solids several times with water till pH neutral, and freeze dry the samples to obtain the imidazolate-derived Ni-N-C catalyst (short for NiNC-IMI). The detailed characterization of the catalyst materials has been presented in recent report[54].

Cathode preparation

We prepared the gas-diffusion electrode for the cathode by spray coating the NiNC-IMI-based catalyst ink onto the microporous layer surface of the gas-diffusion layer prepared from DeNora. (GDL2)[54]. We prepared the catalyst ink by mixing and sonicating 85 mg NiNC-IMI catalyst, Nafion or Sustainion ionomers solutions with 15 wt% or 30 wt % of ionomer with reference to the catalyst mass, 100 µL deionized water, and 2900 µL isopropanol for 15 min.

Anode preparation

The anode is a nickel foam coated with Ni/Fe oxides as prepared according to a prior report by Wang et al.[66]. In brief, we soaked a nickel foam in 3 M HCl aqueous solution overnight, rinsed the foam with deionized water, soaked the foam in an ethanol/isopropanol mixture (50:50 vol%) for 5 min, rinsed it again with deionized water, and then deposit nickel-iron catalyst onto the foam surface by soaking the foam in a solution containing 3.5 mM $Ni(NO_3)_2$ and 1 mM $Fe(NO_3)_3$ for three days. Subsequently, the treated foam was rinsed with deionized water, dried under vacuum for 5 h, and then activated and stored in 1 M KOH solution.

CO_2 electrolysis performance evaluation

The cell was purchased from Dioxide Materials and served to evaluate the performance of the bipolar membrane-based membrane electrode assembly. The cell comprises a cathode, an anode, and a bipolar membrane (Fumasep FBM). A mass flow controller fed the CO_2 channel with a constant flow of humidified CO_2, while a peristaltic pump fed the anolyte channel with KOH aqueous solution at a flow rate of 30 mL min^{-1}. The volume of the anolyte was kept at 100 mL for measurement over different current densities (50–300 mA cm^{-2}), and at 1000 mL for measurement over 150 h stability test at 100 mA cm^{-2}. We applied 50 sccm CO_2 for the cell test of varied current densities, 20 sccm for the stability test.

We also performed electrochemical impedance data for each tested current density. The ohmic and polarisation losses can be determined from the ohmic and polarization resistances and current densities.

The Nernstian shift can be determined as:

$$\eta_N = \frac{2.303 \times \mathrm{RT}}{\mathrm{F}} \times (pH_A - pH_C) \tag{1}$$

Because of the experimental limitations and the local variations of pH across the catalyst layers, it is challenging to accurately determine the pH and the Nernstian shift of the cell. Instead, we used the model to estimate the averaged pH values of the cathode CL and calculate the Nernstian shift caused by the cathode CLs using the equation above.

A potentiostat (VersaST4000) served to perform electrochemical measurements over the cell in a two-electrode configuration, including chronopotentiometry and impedance analyses. We measured the flow rates of the effluent gas streams using a mass flow metre and subsequently analysed their product concentration every 5 min using online gas chromatography (Compact GC). The GC is equipped with molecular sieve 5A columns for two thermal conductivity detectors for hydrogen and carbon monoxide detection. After the electrochemical tests, the analytes were collected for pH measurement by using a pH metre and liquid product analyses by using a nuclear magnetic resonance spectroscopy.

To introduce a PVDF buffer layer, we first sonicated a Merck Omnipore™ membrane filter (0.45 µm pore size, and 65 um in thickness) in deionized water for 5 min, and then placed the membrane filter in between the bipolar membrane and cathode before the cell test.

During the short-term stability test, we monitored the inlet pressure of the cell using a pressure transducer and applied a water (1–2 mL) pulse periodically into the CO_2 channel to wash off the salt precipitation when the inlet pressure increased. The GC injections for the stability took place every 5 h.

The Faradaic efficiency of the gas product was calculated by using the following equation:

$$FE_{product} = \frac{P \times \dot{V} \times c_{product} \times F}{R \times T \times z \times J} \tag{2}$$

Where P is the pressure (101,325 Pa), $\dot{V}$ is the volumetric flow rate, and $c_{product}$ is the volume fraction of the gas product, F is the Faraday constant (96,485 s A mol^{-1}), R is the gas constant (8.314 m^3 Pa $K^{-1}mol^{-1}$), T is the temperature, z is the number of charges transferred to the product, and J is the total current.

The CO_2-calibrated mass flow metre reading can be converted to flow rate by:

$$\dot{V} = \frac{MFM}{C_{CO_2}} \times C_{mix} \tag{3}$$

$$\frac{1}{C_{mix}} = \sum_i \frac{c_i}{C_i} \tag{4}$$

Where MFM is the averaged MFM reading of 30 s duration before the GC injections, C_i is the gas conversion factor for gas i, C_{mix} is the gas conversion factor for the gas mixture, and c_i indicates the volume fraction of the gas i. The gas conversion factor is 0.74 for CO_2, 1.00 for CO, 1.01 for hydrogen, and 0.79 for water vapour.

We used the relative humidity of the outlet flow to estimate the water vapour volume fraction via the below equation:

$$c_{water\ vapor} = \frac{RH \times P_{sat}}{P} \tag{5}$$

Where the RH is the relative humidity, and P_{sat} is the water vapour saturated pressure (2.34 kPa at 20 °C).

The CO_2-to-CO utilization efficiency was calculated from:

$$\varepsilon = \frac{\dot{n}_{CO_2 \to CO}}{\dot{n}_{CO_2,t}} = \frac{\dot{V}_{CO}}{\dot{V}_{CO_2,in} - \dot{V}_{CO_2,out}} \tag{6}$$

Where $\dot{n}_{CO_2 \to CO}$ is the molar flow rate of CO_2 consumed to produce CO, $\dot{n}_{CO_2,t}$ is the molar flow rate of CO_2 consumed within the cell during the reaction, $\dot{V}_{CO}$ is the volumetric CO production rate, $\dot{V}_{CO_2,in}$ is the CO_2 feed rate, and $\dot{V}_{CO_2,out}$ is the CO_2 flow rate in the effluent.

Current density can be calculated by:

$$j = \frac{J}{A} \tag{7}$$

Where A is the active electrode area (5 cm^2).

The partial current density can be obtained via:

$$PCD_{product} = j \times FE_i \tag{8}$$

Determination of the concentration of K^+ and carbonate ions

We determined the concentration of K^+ ions in the anolyte by using the dynamic equivalent point titration technique performed by Metrohm 848 Titrino Plus instrument. Specifically, 20 mL anolyte samples before and after the stability test were continuously stirred in a beaker, where a pH probe was immersed in the solution to record the pH changes while 0.1067 M HCl solution was dosed into the solution via a syringe pump. The volume of HCl dosage was recorded during the titration. The equivalent point is determined from the steepest change

of pH profile as a function of the acid dosage. Because the anolyte after stability contains CO_3^{2-} species, there will be several equivalent points due to the CO_3^{2-}-HCO_3^--H_2CO_3 equilibrium reaction. The equivalent point at pH = ~ 4 indicates that all the anions in the solution were replaced with Cl^- from the acid and helped us estimate the total K^+ concentration in the anolyte. The total K^+ ion concentration can be calculated from the below equation:

$$C_{K^+} = \frac{C_{HCl} \times V_{HCl}}{V_{sample}} \tag{9}$$

Where C_{HCl} represents the concentration of the HCl solution, V_{HCl} represents the acid dosage, and V_{sample} represents the volume of the sample for titration.

To determine the carbonate concentration in the used anolyte, we introduced excess 2 mL 1 M $BaCl_2$ solution into 30 mL anolyte after stability test to remove CO_3^{2-} ions from the liquid system by precipitating all the CO_3^{2-} ions in the form of $BaCO_3$. Because the pH is above 12 for the anolyte after stability test, we can safely conclude that only OH^- and CO_3^{2-} were present in the anolyte. We separated the solid precipitate from the solution by using a centrifuge and collected the supernatant for the titration following the same steps as described above to determine the concentration of OH^-. Then we can estimate the concentration of CO_3^{2-} from the following equations:

$$C_{OH^-} = \frac{C_{HCl} \times V_{HCl}}{V_{sample} \times \frac{30}{32}} \tag{10}$$

$$C_{CO_3^{2-}} = \frac{C_{K^+} - C_{OH^-}}{2} \tag{11}$$

The proportion of current associated with K^+ and CO_2 crossover over total ionic current in the stability test was calculated using the following equations:

$$crossover\ ratio = \frac{z_{ion} \times F \times \Delta n_{ion}}{J \times 3600 \times t} \tag{12}$$

$$\Delta n_{ion} = V_{anolyte,before} C_{ion,before} - V_{anolyte,after} C_{ion,after} \tag{13}$$

The ionic current is the same to the total current J. z_{ion} is the number of charges for the ions: 1 for K^+ and 2 for carbonate ions. Δn_{ion} represents the change in the number of moles of the ions, which is a function of volume of the anolyte before ($V_{anolyte,before} = 1L$) and after ($V_{anoylte,after} = 0.987L$) stability test as well as concentrations of the ions before ($C_{ion,before}$) and after ($C_{ion,after}$) stability test. The concentrations of K^+ and carbonate ions are determined from the titration described above.

Data availability

All data is available in the main text or Supplementary Information. Source data are provided with this paper.

References

1. Samu, A. A. et al. Intermittent Operation of CO(2) Electrolyzers at Industrially Relevant Current Densities. *ACS Energy Lett.* **7**, 1859–1861 (2022).
2. Li, W. et al. Bifunctional Ionomers for Efficient Co-Electrolysis of CO_2 and Pure Water towards Ethylene Production at Industrial-Scale Current Densities. *Nat. Energy* **7**, 835–843 (2022).
3. Wen, G. et al. Continuous CO2 Electrolysis Using a CO_2 Exsolution-Induced Flow Cell. *Nat. Energy* **7**, 978–988 (2022).
4. Hansen, K. U., Cherniack, L. H. & Jiao, F. Voltage Loss Diagnosis in CO_2 Electrolyzers Using Five-Electrode Technique. *ACS Energy Lett.* **7**, 4504–4511 (2022).
5. García de Arquer, F. P. et al. CO(2) electrolysis to multicarbon products at activities greater than 1 A cm^{-2}. *Science* **367**, 661–666 (2020).
6. Rabinowitz, J. A. & Kanan, M. W. The Future of Low-Temperature Carbon Dioxide Electrolysis Depends on Solving One Basic Problem. *Nat. Commun.* **11**, 5231 (2020).
7. Wu, Y. et al. Mitigating Electrolyte Flooding for Electrochemical CO_2 Reduction via Infiltration of Hydrophobic Particles in a Gas Diffusion Layer. *ACS Energy Lett.* 2884–2892 (2022).
8. Disch, J. et al. High-Resolution Neutron Imaging of Salt Precipitation and Water Transport in Zero-Gap CO_2 Electrolysis. *Nat. Commun.* **13**, 6099 (2022).
9. Vass, Á., Kormányos, A., Kószó, Z., Endrődi, B. & Janáky, C. Anode Catalysts in CO_2 Electrolysis: Challenges and Untapped Opportunities. *ACS Catal.* **12**, 1037–1051 (2022).
10. Garg, S. et al. Urea-Functionalized Silver Catalyst toward Efficient and Robust CO(2) Electrolysis with Relieved Reliance on Alkali Cations. *ACS Appl. Mater. Interfaces* **14**, 35504–35512 (2022).
11. Pan, B. et al. Close to 90% Single-Pass Conversion Efficiency for CO2Electroreduction in an Acid-Fed Membrane Electrode Assembly. *ACS Energy Lett.* **7**, 4224–4231 (2022).
12. Huang, J. E. et al. CO(2) electrolysis to multicarbon products in strong acid. *Science* **372**, 1074–1078 (2021).
13. O'Brien, C. P. et al. Single Pass CO2Conversion Exceeding 85% in the Electrosynthesis of Multicarbon Products via Local CO2R-egeneration. *ACS Energy Lett.* **6**, 2952–2959 (2021).
14. Endrődi, B. et al. Operando cathode activation with alkali metal cations for high current density operation of water-fed zero-gap carbon dioxide electrolyzers. *Nat. Energy* **6**, 439–448 (2021).
15. Garg, S., Rodriguez, C. A. G., Rufford, T. E., Varcoe, J. R. & Seger, B. How membrane characteristics influence the performance of CO2and CO electrolysis. *Energy Environ. Sci.* **15**, 4440–4469 (2022).
16. Ren, S. et al. Molecular electrocatalysts can mediate fast, selective CO(2) reduction in a flow cell. *Science* **365**, 367–369 (2019).
17. Larrazábal, G. O. et al. Analysis of Mass Flows and Membrane Cross-over in CO(2) Reduction at High Current Densities in an MEA-Type Electrolyzer. *ACS Appl. Mater. Interfaces* **11**, 41281–41288 (2019).
18. Ma, M., Kim, S., Chorkendorff, I. & Seger, B. Role of ion-selective membranes in the carbon balance for CO(2) electroreduction via gas diffusion electrode reactor designs. *Chem. Sci.* **11**, 8854–8861 (2020).
19. Salvatore, D. A. et al. Designing anion exchange membranes for CO2 electrolysers. *Nat. Energy* **6**, 339–348 (2021).
20. Vass, Á. et al. Local Chemical Environment Governs Anode Processes in CO(2) Electrolyzers. *ACS Energy Lett.* **6**, 3801–3808 (2021).
21. Ma, B., Li, P., Li, W. & Gong, S. What is the clinical significance of the multivariate prediction model for GI stromal tumors with high malignant potential before endoscopic resection? *Energy Environ. Sci.* **13**, 977–985 (2020).
22. Ge, L. et al. Electrochemical CO2 reduction in membrane-electrode assemblies. *Chem* **8**, 663–692 (2022).
23. Hubert, M. A., King, L. A. & Jaramillo, T. F. A non-precious metal hydrogen catalyst in a commercial polymer electrolyte membrane electrolyser. *ACS Energy Lett.* **7**, 17–23 (2022).
24. Dinh, C.-T., García, de Arquer, F. P., Sinton, D. & Sargent, E. H. High Rate, Selective, and Stable Electroreduction of CO2to CO in Basic and Neutral Media. *ACS Energy Lett.* **3**, 2835–2840 (2018).
25. Schultz, H., Bauer, G., Schachl, E., Hagedorn, F. & Schmittinger, P. Ullmann's Encyclopedia of Industrial Chemistry. 978-3-527-30673-2 (John Wiley & Sons, Ltd, 2000)
26. Sassenburg, M., Kelly, M., Subramanian, S., Smith, W. A. & Burdyny, T. Zero-Gap Electrochemical CO(2) Reduction Cells: Challenges

and Operational Strategies for Prevention of Salt Precipitation. *ACS Energy Lett.* **8**, 321–331 (2022).
27. Cofell, E. R., Nwabara, U. O., Bhargava, S. S., Henckel, D. E. & Kenis, P. J. A. Investigation of Electrolyte-Dependent Carbonate Formation on Gas Diffusion Electrodes for CO(2) Electrolysis. *ACS Appl. Mater. Interfaces* **13**, 15132–15142 (2021).
28. Li, M. et al. The role of electrode wettability in electrochemical reduction of carbon dioxide. *J. Mater. Chem. A* **9**, 19369–19409 (2021).
29. Endrődi, B. et al. Multilayer Electrolyzer Stack Converts Carbon Dioxide to Gas Products at High Pressure with High Efficiency. *ACS Energy Lett.* **4**, 1770–1777 (2019).
30. Xu, Y. et al. Self-Cleaning CO2Reduction Systems: Unsteady Electrochemical Forcing Enables Stability. *ACS Energy Lett.* **6**, 809–815 (2021).
31. Kutz, R. B. et al. Sustainion Imidazolium-Functionalized Polymers for Carbon Dioxide Electrolysis. *Energy Technol.* **5**, 929–936 (2017).
32. Liu, Z., Yang, H., Kutz, R. & Masel, R. I. CO2Electrolysis to CO and O2at High Selectivity, Stability and Efficiency Using Sustainion Membranes. *J. Electrochem. Soc.* **165**, J3371–J3377 (2018).
33. Kim, J. Y. et al. Recovering Carbon Losses in CO_2 Electrolysis Using a Solid Electrolyte Reactor. *Nat. Catal.* **5**, 288–299 (2022).
34. Xie, Y. et al. High carbon utilization in CO2 reduction to multi-carbon products in acidic media. *Nat. Catal.* **5**, 564–570 (2022).
35. Monteiro, M. C. O., Philips, M. F., Schouten, K. J. P. & Koper, M. T. M. Efficiency and selectivity of CO(2) reduction to CO on gold gas diffusion electrodes in acidic media. *Nat. Commun.* **12**, 4943 (2021).
36. Bondue, C. J., Graf, M., Goyal, A. & Koper, M. T. M. Suppression of Hydrogen Evolution in Acidic Electrolytes by Electrochemical CO(2) Reduction. *J. Am. Chem. Soc.* **143**, 279–285 (2021).
37. She, Y., Ren, R. & Jiang, N. Mechanical stress can regulate temporomandibular joint cavitation via signalling pathways. *Nat. Energy* **507**, 1–11 (2024).
38. Salvatore, D. A. et al. Electrolysis of Gaseous CO2to CO in a Flow Cell with a Bipolar Membrane. *ACS Energy Lett.* **3**, 149–154 (2018).
39. Eriksson, B. et al. Mitigation of Carbon Crossover in CO2Electrolysis by Use of Bipolar Membranes. *J. Electrochem. Soc.* **169**, 034508 (2022).
40. Yang, K. et al. Cation-Driven Increases of CO(2) Utilization in a Bipolar Membrane Electrode Assembly for CO(2) Electrolysis. *ACS Energy Lett.* **6**, 4291–4298 (2021).
41. Xie, K. et al. Bipolar membrane electrolyzers enable high single-pass CO(2) electroreduction to multicarbon products. *Nat. Commun.* **13**, 3609 (2022).
42. Siritanaratkul, B. et al. Zero-Gap Bipolar Membrane Electrolyzer for Carbon Dioxide Reduction Using Acid-Tolerant Molecular Electrocatalysts. *J. Am. Chem. Soc.* **144**, 7551–7556 (2022).
43. Bui, J. C. et al. Multi-scale physics of bipolar membranes in electrochemical processes. *Nat. Chem. Eng.* **1**, 45–60 (2024).
44. Pärnamäe, R. et al. Bipolar membranes: A review on principles, latest developments, and applications. *J. Membr. Sci.* **617**, 118538 (2021).
45. Patel, A. M., Nørskov, J. K., Persson, K. A. & Montoya, J. H. Efficient Pourbaix diagrams of many-element compounds. *Phys. Chem. Chem. Phys.* **21**, 25323–25327 (2019).
46. Yue, P. et al. Microenvironment Regulation Strategies Facilitating High-Efficiency CO(2) Electrolysis in a Zero-Gap Bipolar Membrane Electrolyzer. *ACS Appl. Mater. Interfaces* **15**, 53429–53435 (2023).
47. Varela, A. S. et al. Electrochemical Reduction of CO2on Metal-Nitrogen-Doped Carbon Catalysts. *ACS Catal.* **9**, 7270–7284 (2019).
48. Möller, T. et al. Efficient CO2to CO electrolysis on solid Ni–N–C catalysts at industrial current densities. *Energy Environ. Sci.* **12**, 640–647 (2019).
49. Ju, W. et al. Understanding activity and selectivity of metal-nitrogen-doped carbon catalysts for electrochemical reduction of CO(2). *Nat. Commun.* **8**, 944 (2017).
50. Weng, L.-C., Bell, A. T. & Weber, A. Z. Modeling gas-diffusion electrodes for CO(2) reduction. *Energy Environ. Sci.* **12**, 1950–1968 (2019).
51. Lees, E. W., Bui, J. C., Song, D., Weber, A. Z. & Berlinguette, C. P. Continuum Model to Define the Chemistry and Mass Transfer in a Bicarbonate Electrolyzer. *ACS Energy Lett.* **7**, 834–842 (2022).
52. Kusoglu, A. & Weber, A. Z. New Insights into Perfluorinated Sulfonic-Acid Ionomers. *Chem. Rev.* **117**, 987–1104 (2017).
53. Wang, J. et al. Design of NiNC single atom catalyst layers and AEM electrolyzers for stable and efficient CO2-to-CO electrolysis: Correlating ionomer and cell performance. *Electrochim. Acta* **461**, 142613 (2023).
54. Brückner, S. et al. Design and diagnosis of high-performance CO2-to-CO electrolyzer cells. *Nat. Chem. Eng.* **1**, 229–239 (2024).
55. Li, Y. C. et al. Bipolar Membranes Inhibit Product Crossover in CO2Electrolysis Cells. *Adv. Sustain. Syst.* **2**, 1700187 (2018).
56. Li, G. et al. Backbone Engineering of Polymeric Catalysts for High-Performance CO_2 Reduction in Bipolar Membrane Zero-Gap Electrolyzer. *Angew. Chem. Int. Ed.* **63**, e202400414 (2024)
57. Siritanaratkul, B., Sharma, P. K., Yu, E. H. & Cowan, A. J. Improving the Stability, Selectivity, and Cell Voltage of a Bipolar Membrane Zero-Gap Electrolyzer for Low-Loss CO2Reduction. *Adv. Mater. Interfaces* **10**, 2300203 (2023).
58. Eagle, C. et al. A manganese complex on a gas diffusion electrode for selective CO2to CO reduction. *Sustain. Energy Fuels* **7**, 2301–2307 (2023).
59. Subramanian, S. et al. Geometric Catalyst Utilization in Zero-Gap CO(2) Electrolyzers. *ACS Energy Lett.* **8**, 222–229 (2022).
60. Bui, J. C., Digdaya, I., Xiang, C., Bell, A. T. & Weber, A. Z. Understanding Multi-Ion Transport Mechanisms in Bipolar Membranes. *ACS Appl. Mater. Interfaces* **12**, 52509–52526 (2020).
61. Oener, S. Z., Foster, M. J. & Boettcher, S. W. Accelerating water dissociation in bipolar membranes and for electrocatalysis. *Science* **369**, 1099–1103 (2020).
62. Chen, L., Xu, Q. & Boettcher, S. W. Kinetics and mechanism of heterogeneous voltage-driven water-dissociation catalysis. *Joule* **7**, 1867–1886 (2023).
63. Peng, J., Tian, M., Cantillo, N. M. & Zawodzinski, T. The ion and water transport properties of K+ and Na+ form perfluorosulfonic acid polymer. *Electrochim. Acta* **282**, 544–554 (2018).
64. Oliva, P. et al. Review of the structure and the electrochemistry of nickel hydroxides and oxy-hydroxides. *J. Power Sources* **8**, 229–255 (1982).
65. Weng, L.-C., Bell, A. T. & Weber, A. Z. Modeling gas-diffusion electrodes for CO(2) reduction. *Phys. Chem. Chem. Phys.* **20**, 16973–16984 (2018).
66. Wang, K. et al. Regulating multiscale structures of nickel-iron-based electrocatalysts for efficient water oxidation. *Cell Rep. Phys. Sci.* **3**, 100870 (2022).

Acknowledgements

M.L. acknowledges the financial support from the Australian Research Council (DE230100637). M.L., W. J., T.B., and P.S. acknowledge the financial support from EU project 851441 – SELECTCO2. W.J. and P.S. acknowledge the support from EU project 101006701 – Ecofuel. J.C.B. was supported in part by a fellowship award under contract FA9550-21-F-0003 through the National Defense Science and Engineering Graduate (NDSEG) fellowship program, sponsored by the Army Research Office (ARO) H-P.I.v.M. and S.S. acknowledge the financing provided for this project in the context of the e-Refinery Institute by Shell Global Solutions International B.V. and the Top Consortia for Knowledge and Innovation (TKI's) of the Dutch Ministry of Economic Affairs. A.Z.W., A.T.B., and J.C.B. all acknowledge support under the Liquid Sunlight Alliance, which is supported by the US Department of Energy, Office of Science, Office of Basic Energy Sciences, Fuels from Sunlight Hub under

award number DE-SC0021266. E.W.L. and A.Z.W. also acknowledge support for the modelling under the CO_2 Consortium funded by BETO in EERE under contract DE-AC02-05CH11231. This project has received funding from the European Research Council (ERC) under the European Union's Horizon 2020 research and innovation programme (Grant Agreement No. Project 101117270).

Author contributions

M.L., E.W.L., and W.J. contributed equally to this work and performed most of the experiments and simulations. M.L. and T.B. conceived the idea and supervised the project. W.J. and P.S. prepared the electrodes. E.W.L., J.C.B., A.Z.W. and A.T.B developed the model and performed the simulation. S.S., K.Y., H.I.v.M., M.A., and J.M. contributed to the electrochemical experiments and characterisations. All authors contributed to the data analyses. M.L., E.W.L., T.B. and W.J. wrote the manuscript with contributions from all authors.

Competing interests

The authors declare no competing interests.

Additional information

Supplementary information The online version contains supplementary material available at https://doi.org/10.1038/s41467-024-52409-z.

Correspondence and requests for materials should be addressed to Mengran Li or Thomas Burdyny.

Peer review information *Nature Communications* thanks Amitava Sarkar and the other, anonymous, reviewers for their contribution to the peer review of this work. A peer review file is available.